J. Fluid Mech. (2023), *vol*. 975, A39, doi:10.1017/jfm.2023.854

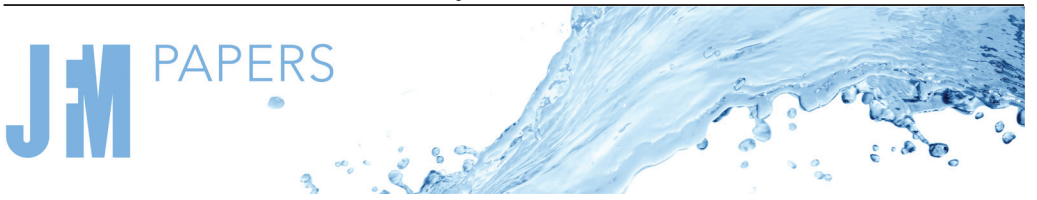

Simultaneous measurements of kinetic and scalar energy spectrum time evolution in the Richtmyer–Meshkov instability upon reshock

Christopher D. Noble[1],†, **Alex M. Ames**[1], **Raymond McConnell**[1], **Jason Oakley**[1], **David A. Rothamer**[1] and **Riccardo Bonazza**[1]

[1]Department of Mechanical Engineering, University of Wisconsin–Madison, Madison, WI 53706, USA

(Received 15 March 2023; revised 25 September 2023; accepted 3 October 2023)

The Richtmyer–Meshkov instability (Richtmyer, *Commun. Pure Appl. Maths*, vol. 13, issue 2, 1960, pp. 297–319; Meshkov, *Fluid Dyn.*, vol. 4, issue 5, 1972, pp. 101–104) of a twice-shocked gas interface is studied using both high spatial resolution single-shot (SS) and lower spatial resolution, time-resolved, high-speed (HS) simultaneous planar laser-induced fluorescence and particle image velocimetry in the Wisconsin Shock Tube Laboratory's vertical shock tube. The initial condition (IC) is a shear layer with broadband diffuse perturbations at the interface between a helium–acetone mixture and argon. This IC is accelerated by a shock of nominal strength Mach number $M = 1.75$, and then accelerated again by the transmitted shock that reflects off the end wall of the tube. An ensemble of experiments is analysed after reshock while the interface mixing width grows linearly with time. The kinetic and scalar energy spectra and the terms of their evolution equation are calculated and compared between SS and HS experiments. The inertial range scaling of the scalar power spectrum is found to follow Gibson's relation (Gibson, *Phys. Fluids*, vol. 11, issue 11, 1968, pp. 2316–2327) as a function of Schmidt number when the effective turbulent Schmidt number is used in place of the material Schmidt number that controls equilibrium scaling. Further, the spatially integrated scalar flux follows similar behaviour observed for the kinetic energy in large eddy simulation studies by Zeng *et al.* (*Phys. Fluids*, vol. 30, issue 6, 2018, 064106) while the spatially varying scalar flux exhibits back scatter along the centre of the mixing layer and forward energy transfer in the spike and bubble regions.

Key words: turbulent mixing, shock waves, transition to turbulence

† Email address for correspondence: cdnoble@arizona.edu

1. Introduction

The Richtmyer–Meshkov (RM) instability (RMI) (Richtmyer 1960; Meshkov 1972) occurs when fluid layers are impulsively accelerated in a direction normal to the interfaces between the layers, leading to the growth of any perturbations. The RMI is seen as a primary cause of inefficiency in attempts to produce energy via inertial confinement fusion (Lindl *et al.* 2004). The capsule and fuel form a material interface, and compression driven by intense X-rays causes the propagation of a shock across this boundary, leading to the mixing of the fuel and capsule material and reducing fusion yield. The instability has also been proposed as an important mechanism by which the mixing of fuel and oxidant in hypersonic aero-engines can be increased (Marble, Hendricks & Zukoski 1989).

The RMI after reshock has been studied extensively over the years. Following are some of the most recent investigations. Initial perturbation effects on the RMI of an inclined plane have recently been explored using numerical simulations by Reilly *et al.* (2015) and Mohaghar, McFarland & Ranjan (2022). Time-resolved particle image velocimetry (PIV) of multi-mode RMI, focused on measuring the growth exponent of the mixing layer width, was performed by Sewell *et al.* (2021). Analytical scalings of the reshocked RMI have been developed by Campos & Wouchuk (2016). A novel oil droplet method was used to extract simultaneous density and velocity measurements of an SF6 gas curtain undergoing RMI (Prestridge *et al.* 2000). Simultaneous planar laser-induced fluorescence (PLIF) and PIV experiments have also explored initial condition effects on RMI growth that show a strong dependence on initial conditions, with Balasubramanian *et al.* (2012) proposing a dimensionless length scale to parameterize this initial condition dependence. Large eddy simulations (LES) of RMI at reshock have been performed with the stretched-vortex subgrid model, allowing estimates of Schmidt number (Sc) effects (Hill, Pantano & Pullin 2006). The influence of different initial perturbation spectrum scalings has been explored by Groom & Thornber (2020), showing the growth rate exponent having a strong dependence on the initial scaling. Simulations have been performed, supporting a series of laser-driven experiments on the National Ignition Facility at Lawrence Livermore National Laboratory, that incorporate high energy density effects into the simulation of the RMI showing non-negligible effects on small-scale mixing by the increased energy transport via thermal electrons (Bender *et al.* 2021). Simultaneous high-speed measurements of reshocked RMI have been collected by Carter *et al.* (2019), where the analysis focused on the exploration of integral quantities. A comprehensive review of the state of the art of RMI studies is presented by Zhou (2017*a*,*b*).

Here, the focus will be on the evolution of spectral quantities, i.e. the scalar and kinetic energy spectra and the terms in their respective transport equations. For brevity, kinetic energy here refers to fluctuating kinetic energy. Integral quantities such as mixing width and mixedness are important metrics that have been used over the years in experiments and numerical simulations. The state-of-the-art diagnostics utilized in the present experiments allow a detailed study of spectral quantities and their evolution.

The study of scale-to-scale energy transport in fluid mechanics has a rich history. Particle image velocimetry experiments exploring two-dimensional energy and enstrophy transfer have been performed by Rivera *et al.* (2003). Turbulent mixing zone integrated scale-to-scale energy transfer specific to RMI turbulence was investigated through simulation by Liu & Xiao (2016) exploring the scale-to-scale flux. Johnson (2020) investigated scale-to-scale flux using a filter-based approach to identify mechanisms driving contributions to the total flux. Structure function transport equations for inhomogeneous turbulence were developed by Gatti *et al.* (2020). The spectral energy

cascade in channel flow was investigated by Andrade *et al.* (2018). Variable density turbulence Karman–Howarth–Monin equations were developed by Lai, Charonko & Prestridge (2018). Energy fluxes and spectra for laminar vs turbulent flow were investigated by Verma *et al.* (2018). Scale space energy density for inhomogeneous turbulence has been explored by Hamba (2018). The integrated kinetic energy spectrum and density fluctuation spectrum in the RMI were studied by Schilling, Latini & Don (2007) and Tritschler *et al.* (2014) using data from numerical simulations. Numerical experiments have explored some of the terms in the transport of kinetic energy in wavenumber space such as in Cook & Zhou (2002) for the Rayleigh–Taylor instability (RTI) case and in Thornber & Zhou (2012) for the RMI case, while a similar experimental study of the combined scalar and kinetic fields has not been performed to date. Energy transfer within a reshocked gas curtain was studied by Zeng *et al.* (2018) calculating the integrated homogeneous flux of kinetic energy. Here, the focus is on the transport of scalar energy; however, a similar behaviour of the flux is observed.

Investigations of scalar mixing, both active and passive, have been the subject of intense study. For idealized turbulent mixing and arbitrary Schmidt number mixing, Corrsin (1957, 1964) developed scaling relations. Passive scalar mixing in shock–turbulence interactions was explored through simulations (Gao, Bermejo-Moreno & Larsson 2020). Low Schmidt number turbulent spectra were generated by Yeung & Sreenivasan (2013) and then low Schmidt number mixing with a mean gradient was further explored by Yeung & Sreenivasan (2014). Structure functions at low Schmidt number with a mean gradient were investigated by Iyer & Yeung (2014). A spectral theory of scalar fields mixed by turbulence was assembled by Gibson (1968). Generalized scale-to-scale budget equations for anisotropic scalar turbulence as a function of Schmidt number were explored by Gauding *et al.* (2014). The probability distribution of passive scalars in grid generated turbulence was investigated by Jayesh & Warhaft (1991) with the skewness and kurtosis of diffusing scalars being modelled by Schopflocher & Sullivan (2005). Scaling exponents for active scalars were developed by Constantin (1998). Incompressible Rayleigh–Taylor (RT) turbulent mixing was investigated by Boffetta & Mazzino (2017). Anomalous scalings of active scalars in homogeneous turbulence were developed by Ching & Cheng (2008). Kinetic and scalar structure function scaling laws for RMI turbulence have been investigated through simulations and theory by Zhou *et al.* (2023). The Batchelor spectrum of passive scalar isotropic turbulence was discussed by Donzis, Sreenivasan & Yeung (2010). The difference between active vs passive scalar turbulence scaling has been explored by Celani *et al.* (2002, 2004). Moving to spatially developing turbulence, passive scalar statistics were measured by Paul, Papadakis & Vassilicos (2018). Applying self-similar scaling to RT turbulence, growth rates and scaling relations were found by Ristorcelli & Clark (2004). Schmidt number effects in compressible turbulent mixing have been elucidated by Ni (2015). The scalar energy spectrum has been explored in a number of experimental studies. Weber *et al.* (2014) and Reese *et al.* (2014) looked at the evolution of the scalar spectrum for the currently considered initial condition (IC) after a single shock and found a small but growing wavenumber range with a $-\frac{5}{3}$ Kolmogorov scaling. Previous high-speed PLIF experiments (Noble *et al.* 2020*a*,*b*) using this IC lacked direct measurement of the velocity field so they were not suitable to extract individual production and transport terms. This is remedied in the present work, where the production and flux terms can be separately evaluated. Here, we will present an argument that the canonical isotropic homogeneous turbulent scaling of Gibson (1968) may be applicable to inhomogeneous anisotropic RMI turbulence when the non-equilibrium effective *Sc* is used in place of the material *Sc* that controls equilibrium scaling.

	M_s	A_s
HS	1.75 ± 0.09	0.52 ± 0.098
SS	1.89 ± 0.05	0.42 ± 0.04

Table 1. Parameters of HS and SS experiments. Here, M_s is the Mach number of the 1st shock and A_s is the initial Atwood number.

2. Experiment details

Experiments are conducted in a 9.1 m long, vertical, downward-firing shock tube with a square internal cross-section (25.4 cm on a side). The facility is described in detail by Anderson *et al.* (2000), while figure 1 of Noble *et al.* (2020*a*) shows a diagrammatic layout of the shock tube and test section specifically. The process for generating the current IC is described in detail by Noble *et al.* (2020*a*). This IC has been used in previous studies in this facility (Reese *et al.* 2014; Weber *et al.* 2014; Noble *et al.* 2020*a*,*b*). The high-speed (HS) series is composed of 20 individual experiments, while the single-shot (SS) series is composed of 71 individual experiments. Parameters for both experiments are presented in table 1. For the HS simultaneous PLIF and PIV (HS) experiments, a pulse-burst laser system is used to create a pulse train of 10 ms duration at a repetition rate of 20 kHz. The system amplifies the output of an Nd:YVO_4 oscillator laser in diode-pumped Nd:YAG amplification stages. The second and fourth harmonics at 532 and 266 nm, respectively, are used in the experiments with an average total energy of 80 mJ per pulse. The pulse train is focused by a spherical and a cylindrical lens to create a diverging laser sheet that spans the entire width of the shock tube, 1 m above the end wall of the tube. The 266 nm laser sheet excites the acetone present in the light gas mixture causing it to fluoresce while the 532 nm sheet is Mie scattered by TiO_2 particles with a nominal diameter of 300 nm injected above, below and in the centre of the mixing layer. A HS camera (Phantom V1840) with a 1 μs exposure is used to capture the resulting fluorescence signal while a second HS camera (Photron Fastcam SA-Z) captures the resulting Mie-scattered light. Figure 1 shows the required field of view for the PIV camera to allow a similar PIV resolution between HS and SS experiments. For the SS simultaneous PLIF and PIV experiments, a dual-head Nd:YAG laser (Ekspla NL303D) is used to generate two 532 nm pulses at 260 mJ pulse^{-1} and an excimer laser is used to generate a single pulse of 308 nm light at 360 mJ pulse^{-1}. These pulses are combined using a dichroic beam splitter and then passed through the same sheet-generating optics. A CCD camera (Lavision Flowmaster 3S3D) was used to capture the resulting PLIF signal and an interline transfer CCD camera (TSI PIV01440, 29 MP) was used to record the PIV images.

Figure 2 shows a $z - t$ diagram generated using measured wave speeds. The blue solid line denotes the material interface between the light and heavy gases. The dashed black lines show the spatial extents of the imaging window while the shaded region marks the space–time boundaries of the field of view for the extracted concentration field. The symbols denote the four reshock times explored in the SS experiments.

For both SS and HS experiments the PLIF and PIV images are registered onto each other following the procedure described in Reese *et al.* (2014) to ensure the velocity and concentration fields are available at the correct physical points.

The PIV particle images were processed using PIVLab (Thielicke & Sonntag 2021), using recursive grid refinement from a 128×128 px window down to a smallest window of 16×16 px (50 % overlap). A $3 \times 3 \times 3$ spatio-temporal median filter was used for

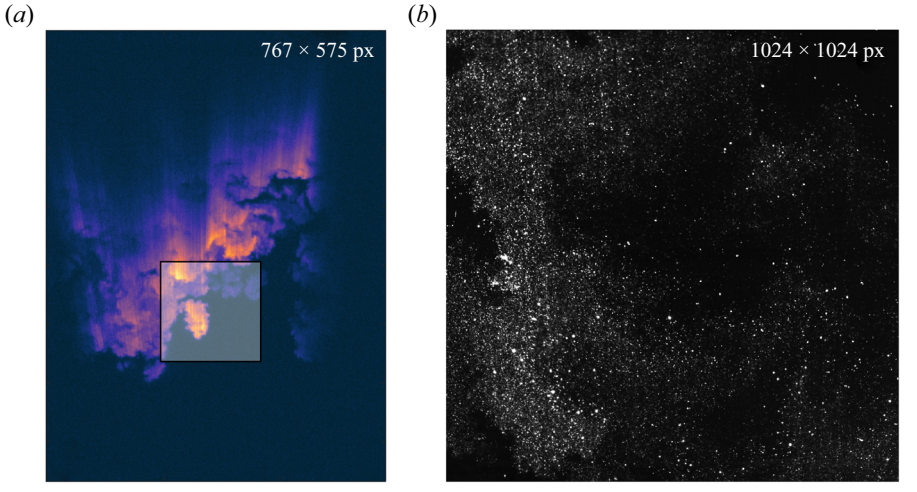

Figure 1. (*a*) Example high-speed (HS) PLIF image. The PIV image subdomain required to acquire actionable PIV images at high speed is highlighted. (*b*) Example PIV raw image from HS experiments.

	t_s (ms)	t_{rs} (ms)	Sym
IC	0	–	
*RS*1	2.3	0.26	
*RS*2	3.07	1.14	
*RS*3	3.87	1.92	
*RS*4	4.7	2.75	

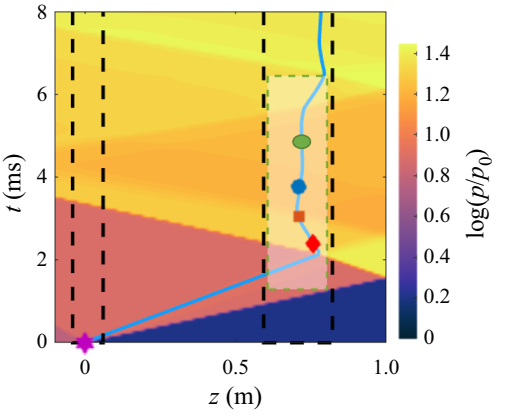

Figure 2. Experimental $z-t$ diagram with window locations shown with dashed black lines, the interface location in blue and HS PLIF FOV shown as the highlighted rectangle. Individual symbols refer to single-shot (SS) times. Here, $t=0$ and $z=0$ refer to the time and space location of the initial shock–interface interaction; t_s denotes the time after shock and t_{rs} is the time after reshock; $RS1-4$ are the labels for the four post reshock times investigated in the SS experiment campaign.

outlier detection, vector replacement and Gaussian smoothing (to remove high frequency noise) in the PIV vector fields.

These set-ups result in effective resolutions, after image registration, of $\Delta x = 0.43$ mm px^{-1} for the HS experiments and $\Delta x = 0.22$ mm px^{-1} for the SS experiments. Estimates of PIV uncertainty using correlation peak-to-peak ratio relations developed in Charonko & Vlachos (2013) lead to an uncertainty distribution shown in figure 3. The distribution has a median of 0.9 % and a mean of 3.7 %.

3. Analysis methodology

The process described in Noble *et al.* (2020*a*) to transform the scalar transport equation is applied to the z-momentum transport equation.

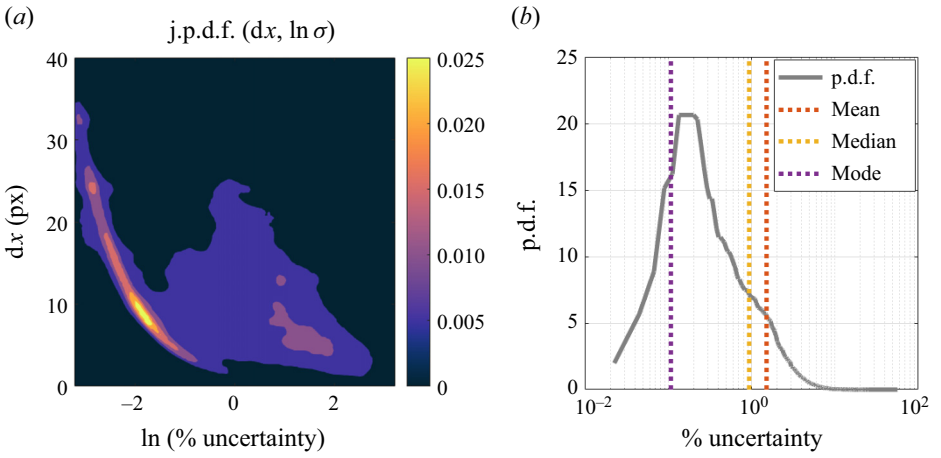

Figure 3. (*a*) Joint probability density function (j.p.d.f.) of displacement and % displacement uncertainty, (*b*) p.d.f. of estimated % PIV uncertainty.

Indicating the concentration with ξ, the functional form of this transformation is $\xi(x, z, t) \rightarrow \xi(x^+, z^+, h^+)$ with $x^+ = x/W$, $z^+ = (z - z_0)/h$ and $h^+ = h/h_0$ where x is the spanwise coordinate and z is the streamwise coordinate, W is a representative spanwise length scale (here, the shock tube width), $z_0 = 4\int_{-\infty}^{\infty} z\bar{\xi}(1-\bar{\xi})\,\mathrm{d}z^+$ is the time-varying location of the mole-fraction-weighted centroid of the mixing layer, h is the time-varying mixing thickness defined below and h_0 is the initial mixing thickness immediately after the reflected shock has fully traversed the mixing layer. Introducing the spanwise average in the x-direction of a function f as

$$\bar{f} = \frac{1}{W}\int_0^W f\,\mathrm{d}x, \tag{3.1}$$

such that $f = \bar{f} + f'$, then the mixing thickness is defined as

$$h = 4\int_{-\infty}^{\infty} \bar{\xi}(1-\bar{\xi})\,\mathrm{d}z. \tag{3.2}$$

Starting with the transport equation for ρw,

$$\frac{\partial \rho w}{\partial t} + \nabla\cdot\rho\boldsymbol{u}w = -\frac{\partial p}{\partial z} + \nabla\cdot\mu\nabla w, \tag{3.3}$$

where $\boldsymbol{u}$, p and μ are the velocity, pressure and kinematic viscosity, respectively, and w is the vertical (streamwise) component of the velocity. Specializing to two dimensions, and introducing the following non-dimensionalization

$$\boldsymbol{u}^+ = \frac{\boldsymbol{u} - \boldsymbol{V_0}}{\dot{h}}, \tag{3.4}$$

where V_0 is the bulk velocity of the interface in the laboratory-fixed frame, (3.3) becomes

$$\frac{\partial \rho^+ w^+}{\partial \ln h^+} - z^+\frac{\partial \rho^+ w^+}{\partial z^+} + \frac{\partial \rho^+ u^+ w^+}{\partial x^+}\frac{h}{W} + \frac{\partial \rho^+ w^+ w^+}{\partial z^+}$$

$$= \frac{-1}{\gamma M_h^2}\frac{\partial p^+}{\partial z^+} + \frac{1}{Re_h}\left[\frac{\partial \mu^+}{\partial x^+}\frac{\partial w^+}{\partial x^+}\left(\frac{h}{W}\right)^2 + \frac{\partial \mu^+}{\partial z^+}\frac{\partial w^+}{\partial z^+}\right]$$
$$+ \frac{\mu^+}{Re_h}\left[\frac{\partial^2 w^+}{\partial x^{+2}}\left(\frac{h}{W}\right)^2 + \frac{\partial^2 w^+}{\partial z^{+2}}\right]. \tag{3.5}$$

The scalar version of this transport equation was derived in Appendix A of Noble *et al.* (2020*a*) and is the form used by Ristorcelli & Clark (2004). The shock tube width (W) is used as the normalization for the spanwise length scale. The IC generation is directly linked to the geometry of the shock tube, although, due to the size of the tube, the RM evolution is not further affected by the shock tube width. Here, $Re_h = \rho_0 h\dot{h}/\mu_{mix}$ is the outer scale Reynolds number, and $M_h = \dot{h}/a$ is the outer-scale Mach number, with a being the speed of sound in the light gas. This parameter appears here due to the normalization of the pressure term in the momentum transport equation. The outer-scale Mach number is not further considered as a dominant parameter due to compressibility effects having been found to be negligible until larger shock strengths where post-shock fluctuating Mach numbers grow above around 0.3; here, the fluctuating Mach number is of the order of 0.1. Further, μ_{mix} is the dynamic viscosity of the mixture, $\rho^+ = \rho/\rho_0 = 1 + (R-1)\xi$ is the normalized density with $R = (1+A)/(1-A)$ being the density ratio, $p^+ = p/(\rho_0 \dot{h}^2)$ is the normalized pressure and $\mu^+ = \mu/\mu_{mix}$ is the normalized viscosity. Following the procedure in Tritschler *et al.* (2014), μ is calculated using multi-component mixing rules that use the Chapman–Enskog model to calculate pure gas transport coefficients. The viscosity, μ_{mix}, is then the mass average of the bulk values of μ.

3.1. *Power spectrum evolution*

Starting with (3.5) and following Thornber & Zhou (2012) by introducing $\boldsymbol{v}_i = \sqrt{\rho^+}\boldsymbol{u}_i^+$ and the transformed scalar equation from (Noble *et al.* 2020*a*), taking the Fourier transform, $\hat{\xi} = \mathcal{F}_{x^+}[\xi]$, and multiplying by the respective complex conjugates $\hat{\xi}^*$, the evolution equations for the scalar energy spectrum ($E_\xi = \hat{\xi}\hat{\xi}^*$) and the density-weighted kinetic energy spectrum ($E_w = \widehat{\boldsymbol{v}_3}\widehat{\boldsymbol{v}_3}^*$) become

$$\frac{\partial E_\xi}{\partial \ln h^+} - z^+\frac{\partial E_\xi}{\partial z^+} + \mathcal{P} + \mathcal{T}_{x\xi} + \mathcal{T}_{z\xi} = \mathcal{D}_{x\xi} + \mathcal{D}_{z\xi} - \chi_\xi \tag{3.6a}$$

$$\frac{\partial E_w}{\partial \ln h^+} - z^+\frac{\partial E_w}{\partial z^+} + \mathcal{T}_{xw} + \mathcal{T}_{zw} = -\mathcal{H}_w + \Gamma_x + \Gamma_z + \mathcal{D}_{xw} + \mathcal{D}_{zw}, \tag{3.6b}$$

with all terms defined in table 2. The Schmidt number $Sc = \mu/\rho\mathcal{D}$ is calculated similarly to μ using the multi-component mixing rules described in Tritschler *et al.* (2014).

This is a similar form to the transport equation of the inhomogeneous kinetic energy spectrum found by Andrade *et al.* (2018). The terms in the scalar transport equation are then integrated over dimensionless time ($\ln h^+$) to the latest time available in all experiments, $h^+ = 5$, resulting in (A2)–(A6). These allow an analysis of the different contributions to the change in the power spectra over the linear growth regime.

This leads to a form of the power spectra that has been integrated over dimensionless time. Each of the terms can be considered separately to identify its contribution to the total

	E_ξ	E_w
Production $\mathcal{P}$	$\beth[w^+, \xi]\frac{\partial \bar{\xi}}{\partial z^+}$	N/A
Transport $\mathcal{T}_x$	$\frac{h}{W}\beth\left[\frac{\partial u^+\xi}{\partial x^+}, \xi\right]$	$\frac{1}{2}\frac{h}{W}\beth\left[\frac{1}{\sqrt{\rho^+}}\frac{\partial v_1 v_3}{\partial x^+}, v_3\right]$
Transport $\mathcal{T}_z$	$\beth\left[\frac{\partial w^+\xi}{\partial z^+}, \xi\right]$	$\frac{1}{2}\beth\left[\frac{1}{\sqrt{\rho^+}}\frac{\partial v_3 v_3}{\partial z^+}, v_3\right]$
Pressure $\mathcal{H}_w$	N/A	$\frac{1}{\gamma M_h^2}\beth\left[\frac{1}{\sqrt{\rho^+}}\frac{\partial p^+}{\partial z^+}, v_3\right]$
Diffusivity gradient Γ_x	N/A	$\left(\frac{h}{W}\right)^2\frac{1}{Re_h}\beth\left[\frac{1}{\sqrt{\rho^+}}\frac{\partial \mu^+}{\partial x^+}\frac{\partial w^+}{\partial x^+}, v_3\right]$
Diffusivity gradient Γ_z	N/A	$\frac{1}{Re_h}\beth\left[\frac{1}{\sqrt{\rho^+}}\frac{\partial \mu^+}{\partial z^+}\frac{\partial w^+}{\partial z^+}, v_3\right]$
Diffusion $\mathcal{D}_x$	$\frac{-2k^{+2}}{Re_h Sc}\left(\frac{h}{W}\right)^2 E_\xi$	$\left(\frac{h}{W}\right)^2\frac{1}{Re_h}\beth\left[\frac{1}{\sqrt{\rho^+}}\mu\frac{\partial^2 w^+}{\partial x^{+2}}, v_3\right]$
Diffusion $\mathcal{D}_z$	$\frac{1}{Re_h Sc}\left[\frac{\partial^2 E_\xi}{\partial z^{+2}}\right]$	$\frac{1}{Re_h}\beth\left[\frac{1}{\sqrt{\rho^+}}\mu\frac{\partial^2 w^+}{\partial z^{+2}}, v_3\right]$
Dissipation χ	$\frac{1}{Re_h Sc}\left[\frac{\partial \hat{\xi}}{\partial z^+}\frac{\partial \hat{\xi}^*}{\partial z^+}\right]$	N/A

Table 2. Terms in scalar and kinetic energy spectrum transport, where $\beth[F, G] = \hat{F}^*\hat{G} + \hat{F}\hat{G}^*$.

change in energy,

$$\Delta E_\xi = P_\xi - T_{x\xi} - \frac{\partial \Pi_{z\xi}}{\partial z^+} + D_{x\xi} + D_{z\xi} + X_\xi. \tag{3.7}$$

Alternatively, the scalar transport equation can be integrated over the inhomogeneous direction to investigate the evolution of the total scalar energy as a function of wavenumber and time,

$$\frac{\partial \Lambda_\xi}{\partial \ln h^+} = \hat{P}_\xi + \hat{T}_\xi + \hat{D}_\xi + \hat{X}_\xi. \tag{3.8}$$

The terms are defined explicitly also in (A2)–(A6) in the Appendix.

3.2. *Spectral bandwidth and distribution*

Here, the bandwidth of both the scalar spectrum and the density-weighted kinetic spectrum are defined to provide a coarse measure of how energy is distributed between scales

$$Re_\tau Sc_\tau = \left(\frac{L}{\lambda}\right)^2_\xi = \frac{\left(\int \frac{E_\xi}{k}\,\mathrm{d}k\right)^2\left(\int E_\xi k^2\,\mathrm{d}k\right)}{\left(\int E_\xi\,\mathrm{d}k\right)^3}, \tag{3.9a}$$

$$Re_\tau = \left(\frac{L}{\lambda}\right)_w^2 = \frac{\left(\int \frac{E_w}{k}\,\mathrm{d}k\right)^2 \left(\int E_w k^2\,\mathrm{d}k\right)}{\left(\int E_w\,\mathrm{d}k\right)^3}, \tag{3.9b}$$

where $L = \int E/k\,\mathrm{d}k / \int E\,\mathrm{d}k$ is the integral scale of a given spectrum and $\lambda^2 = \int E\,\mathrm{d}k / \int k^2 E\,\mathrm{d}k$ is the Taylor scale. Also, Re_τ is an effective 'turbulence' Reynolds number and Sc_τ is an effective 'turbulence' Schmidt number

$$Sc_\tau = \left(\frac{L}{\lambda}\right)_\xi^2 \left(\frac{\lambda}{L}\right)_w^2. \tag{3.10}$$

The definitions of Re_τ and $Re_\tau Sc_\tau$ here come from homogeneous isotropic turbulence (HIT) and describe the bandwidth of the respective spectra. This is a measure of the breadth of wavenumber space accessed. Here, Sc_τ becomes a measure of the difference in bandwidth between the scalar spectrum and the kinetic spectrum. In HIT, where a statistical equilibrium is reached, the material Schmidt number would determine the behaviour of the scalar spectrum compared with the kinetic energy spectrum. In the present case, the system cannot be said to be at equilibrium, thus the material Schmidt number does not necessarily prescribe how the scalar spectrum behaves. Therefore, the instantaneous effective turbulent Schmidt number Sc_τ is used here in place of the material Schmidt number.

The spectral slopes are defined as

$$\zeta_\xi = \left.\frac{\partial \ln E_\xi}{\partial \ln k}\right|_{k=k_{\lambda_\xi}}, \tag{3.11a}$$

$$\zeta_w = \left.\frac{\partial \ln E_w}{\partial \ln k}\right|_{k=k_{\lambda_w}}, \tag{3.11b}$$

where the derivatives are taken at the Taylor microscale wavenumber, so within the inertial–convective range. These slopes provide another coarse description of how energy is distributed within wavenumber space.

4. Results and discussion

The results presented here are derived from data obtained according to the methodology described in § 2. The set of 20 HS and 71 SS experiments are analysed according to the theory constructed in § 3.

Figure 4 shows an example of the interface evolution captured in a HS experiment run, showing snapshots as a function of time every 5 frames.

4.1. *Power spectra*

Following Schilling & Latini (2010), the power spectra are integrated over the mixing layer such that $\Lambda_\xi(k_x^+, h^+) = \int_{-\infty}^{\infty} E_\xi\,\mathrm{d}z^+$ (here, the limits are $\pm\infty$ rather than the bubble and spike heights although, in practice, the limits are the bounds of the field of view of the experiment). The parameter Λ_ξ, shown in figure 5(*a*), is a measure of the magnitude of fluctuations at a given wavenumber with a smaller magnitude indicating

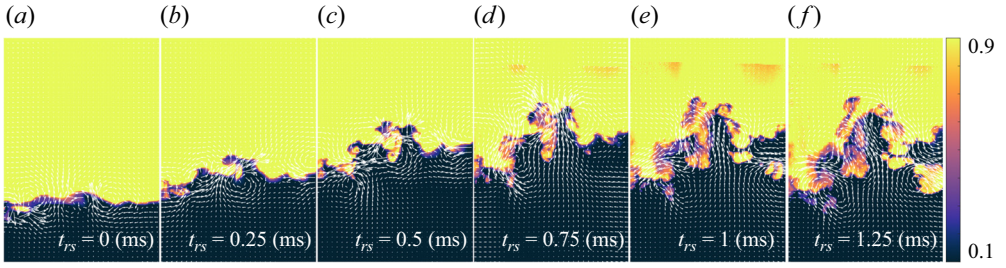

Figure 4. Example evolution of the mixing layer after reshock. The light gas (He + Acetone) mole fraction is shown overlaid with two-dimensional velocity vectors.

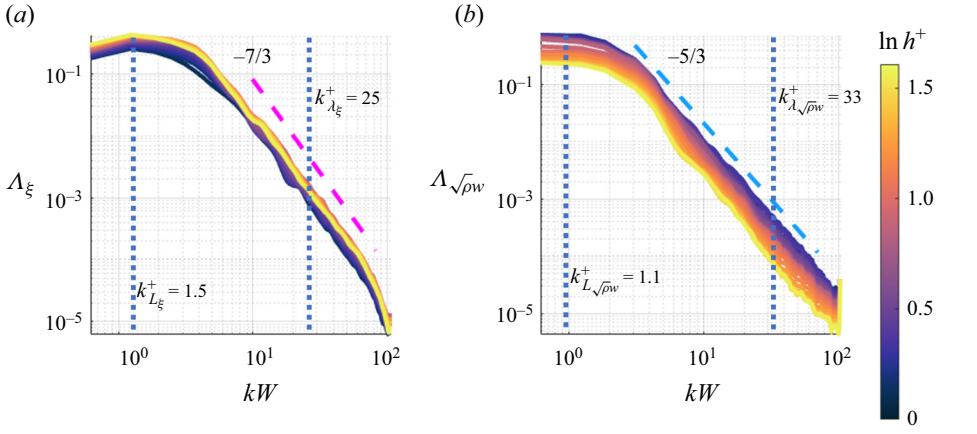

Figure 5. Ensemble HS integrated power spectra. (*a*) Integrated scalar power spectrum. (*b*) Integrated kinetic power spectrum. Here, h^+ plays the role of time for this mixing system. Integration is performed in the inhomogeneous direction.

weaker fluctuations from the mean and a more fully mixed state and Λ_w is a measure of the kinetic energy at a given wavenumber, and is shown in figure 5(*b*).

For both Λ_ξ and Λ_w, energy is concentrated at smaller wavenumbers around the integral scale. A steady increase in energy over time is seen in Λ_ξ, showing a growth in bulk structures. For Λ_w a deposition of kinetic energy is seen followed by a slow decay. A similar behaviour can be seen in figure 12 of Tritschler *et al.* (2014) and figure 5(*a*) of Carter *et al.* (2019).

Figure 6 explores the coarse measures of the spectra introduced in § 3.2. Figures 6(*a*) and 6(*c*) show joint probability density functions (j.p.d.f.s) and figures 6(*b*) and 6(*d*) show conditional probability density functions (c.p.d.f.s).

In particular, figure 6(*a*) shows the j.p.d.f. of the turbulent Schmidt number and the scalar spectral slope. A peak in the j.p.d.f. can be seen where the scalar slope is approximately between $-8/3$ and $-10/3$ and the turbulent Schmidt number is between 0.3 and 0.4, which aligns with the estimate of the material Schmidt number of 0.3. Figure 6(*b*) shows the c.p.d.f., which represents what the expected spectral slope is for a given turbulent Schmidt number. The result here is close to the interpolation formula by Gibson (1968) ((46) in that paper), providing some encouragement to the proposition made in § 3.2 that, with the flow being far from HIT, the turbulent Schmidt number is appropriate to use in place of the material Schmidt number to determine expected behaviour.

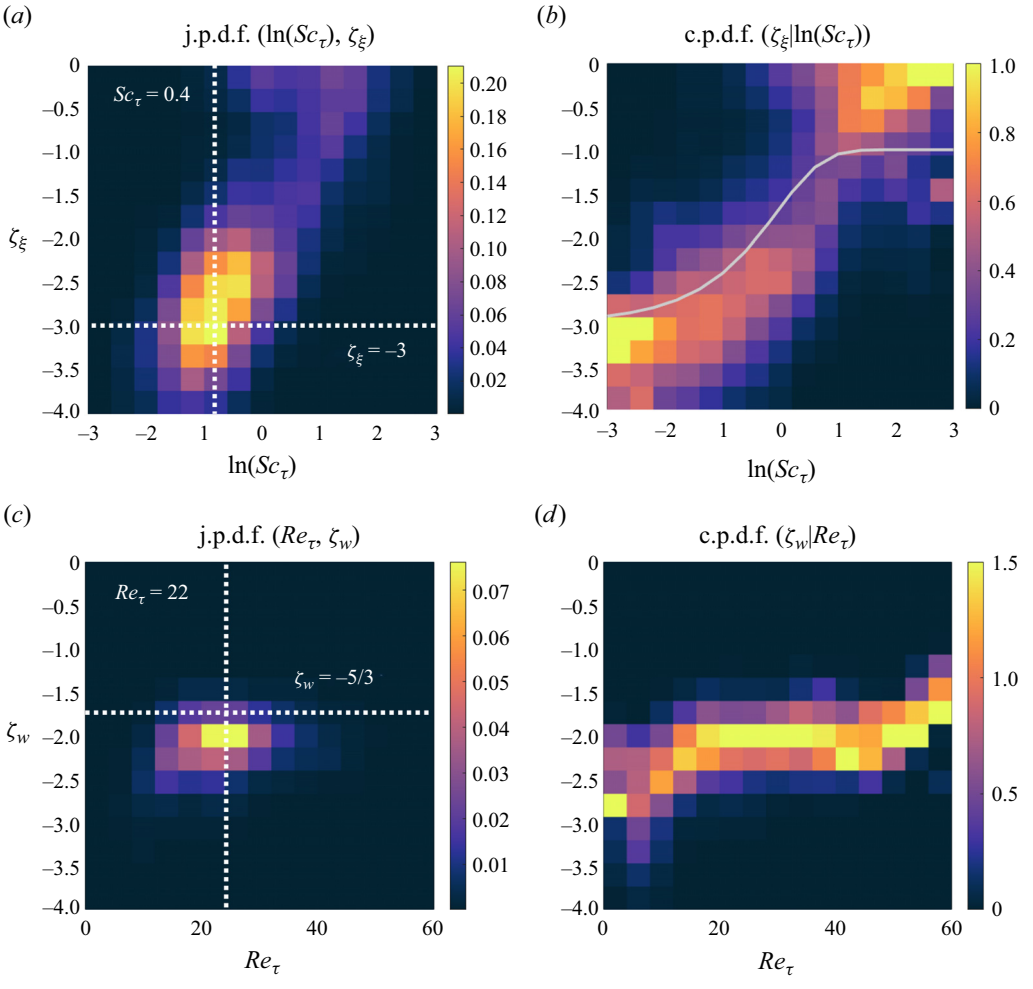

Figure 6. The HS results: (*a*) j.p.d.f. of spectral Schmidt number and scalar spectral slope; (*b*) conditional p.d.f. of scalar spectral slope given a spectral Schmidt number. (White line: Gibson 1968, (46).) (*c*) The j.p.d.f. of the spectral Reynolds number and the kinetic spectral slope. (*d*) Conditional p.d.f. of the spectral Reynolds number and the kinetic spectral slope.

Figure 6(*c*) shows the j.p.d.f. of turbulent Reynolds number and kinetic spectral slope. A peak can be seen at a slope between $-5/3$ and -2 at an Re_τ between 20 and 25. The c.p.d.f. in figure 6(*d*) points to a weak dependence of the kinetic spectral slope on the turbulent Reynolds number, although it is difficult to draw conclusions at the lowest and highest Re_τ due to the lower number of observations available to generate the distribution there due to the turbulent Reynolds number over all measurements being close to the peak.

Figure 7 shows the same measurement as figure 6 but for the SS data set. Very similar structures and values and trends are visible in the Schmidt number-based plots, 7(*a*) and 7(*b*). The Reynolds number-based plots show a peak at a slightly lower value than the HS results in plot 6(*c*). Figure 7(*d*) shows a similar trend for the small Re_τ range; however, a similar problem occurs with fewer instances to produce statistics for the higher Re_τ values.

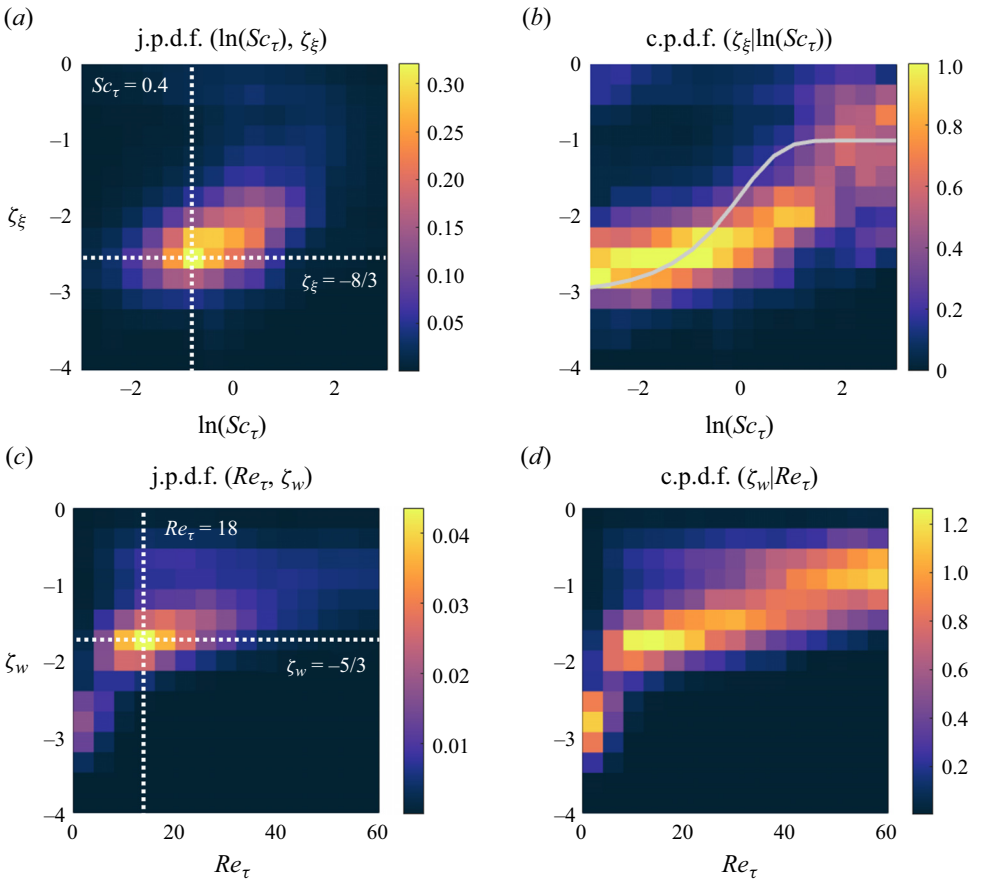

Figure 7. The SS results: (*a*) j.p.d.f. of spectral Schmidt number and scalar spectral slope; (*b*) conditional p.d.f. of scalar spectral slope given a spectral Schmidt number. (White line: Gibson 1968, (46).) (*c*) The j.p.d.f. of the spectral Reynolds number and the kinetic spectral slope. (*d*) Conditional p.d.f. of the spectral Reynolds number and the kinetic spectral slope.

4.2. *Partition of energy*

Equation (3.7) describes the partition of the change in scalar energy over a given time interval. For this study, the dimensionless time interval is the regime of linear growth of the mixing width for all experiments from $\ln h^+ = 0$ to $\ln h^+ = 1.6$. The individual terms are plotted in figure 8 and defined in the Appendix. The time period represented here begins after the reflected shock has fully traversed the mixing layer; it includes the passage of an expansion wave and ends at the latest dimensionless time available before the arrival of a compression wave from above. This analysis is only possible with the time-resolved HS data set.

The total increase in energy, i.e. the increase in fluctuations away from the spanwise mean, ΔE_ξ, is concentrated at larger wavelengths, of the order of the shock tube width, which correspond to the growth and transport of bulk structures. This is evident in the plot of the production term P_ξ, which represents the transfer of energy from the mean gradient of the scalar field to the fluctuations via the correlation of streamwise velocity fluctuations and scalar fluctuations. The homogeneous transport term $T_{x\xi}$ describes how energy is transported in wavenumber space, where above and below the interface energy

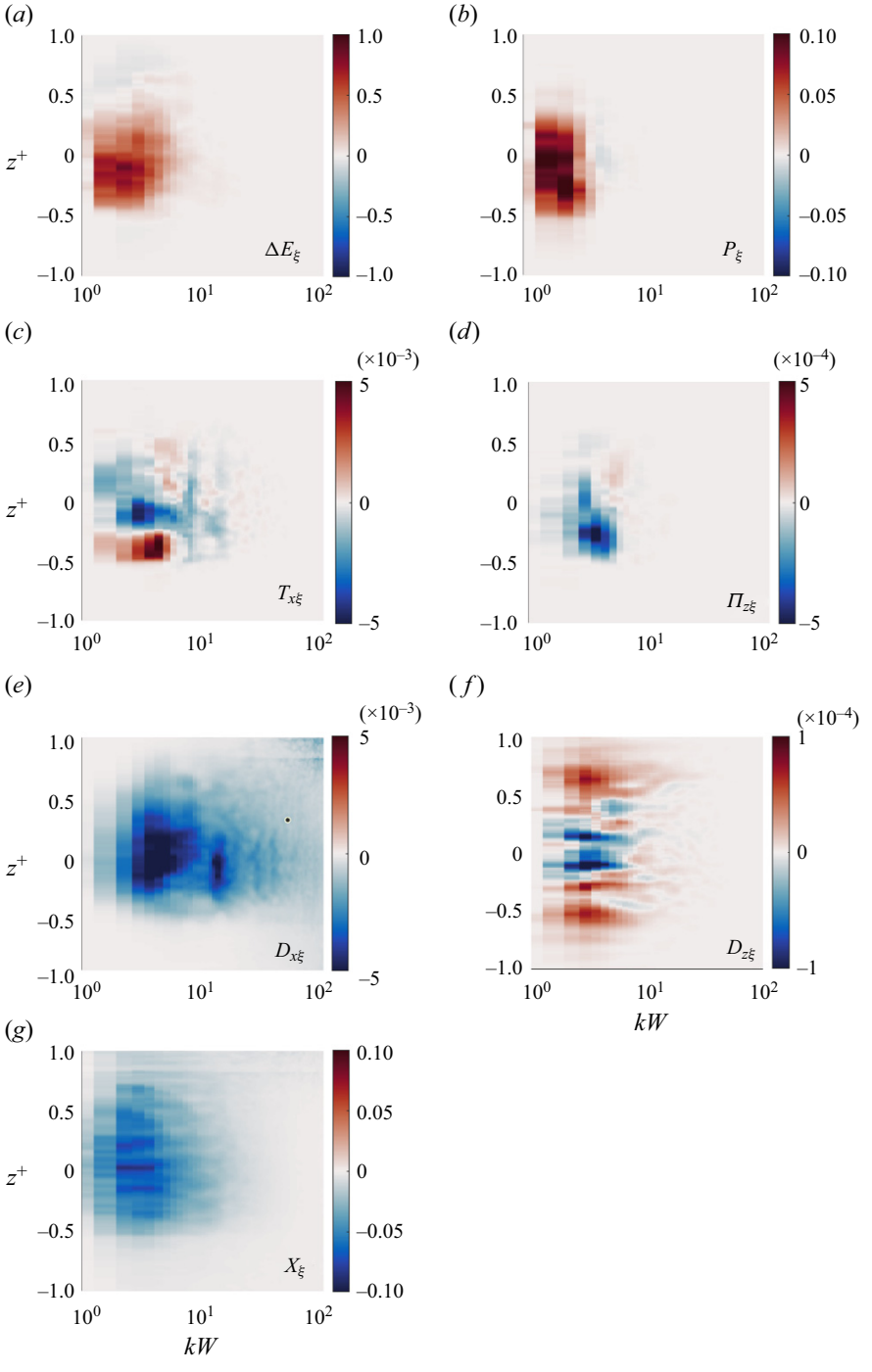

Figure 8. The terms of the transport of fluctuating scalar energy (3.7) over the linear growth regime from $h/h_0 = 1$ to 5 for the HS data set. Here, ΔE_ξ is the change in scalar energy over linear growth regime, P_ξ is the production of scalar energy, $T_{x\xi}$ is the homogeneous convective transport, $\Pi_{z\xi}$ is the inhomogeneous convective flux, $D_{x\xi}$ is the homogeneous diffusion term, $D_{z\xi}$ is the inhomogeneous diffusion term and X_ξ is the dissipation.

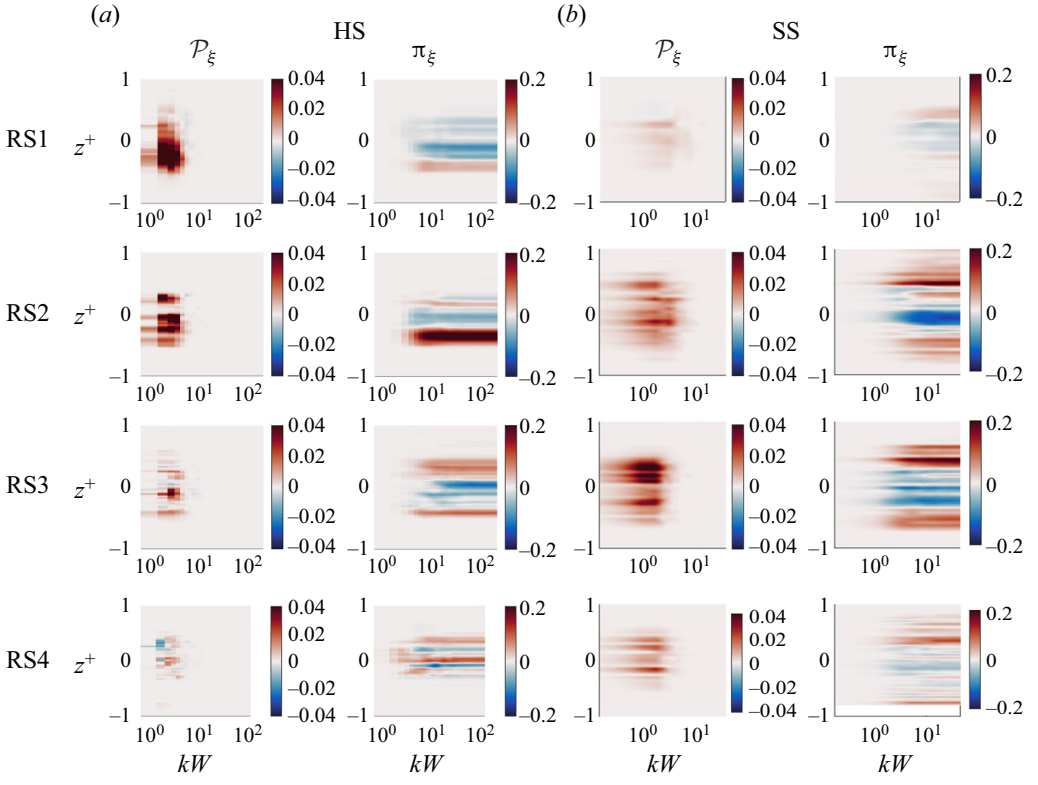

Figure 9. Comparison of the production and transport flux between HS and SS experiments at comparable experiment times.

is being transported from larger wavelengths to smaller wavelengths ($T_{x\xi} < 0$) while in the centre of the mixing layer energy is being transported to larger wavelengths ($T_{x\xi} > 0$). The inhomogeneous transport flux $\Pi_{z\xi}$ shows how scalar energy is transported away from the centre of the mixing layer with a larger amount of energy transported in the negative z-direction than toward the positive z-direction above the interface. This asymmetry in energy transport is seen in Thornber & Zhou (2012) and is explained as an Atwood number effect. The homogeneous diffusion, $D_{x\xi}$ measures the rate of diffusing scalar energy from large to small wavelengths, while the inhomogeneous diffusion term $D_{z\xi}$ describes how energy is diffused in the vertical direction. The form makes sense as roughly the second derivative of a Gaussian such that energy is taken from the centre of the mixing layer and diffused to above and below the interface. Here, X_ξ is the dissipation term and represents the removal of scalar energy which appears to occur at longer wavelengths where the gradients are largest.

4.3. *Time evolution*

To compare the HS and SS data sets further, here, the time evolution of the production and homogeneous transport terms are shown in figure 9.

The same structures as discussed in § 4.2, referring to figure 8, appear here, where production occurs around the centroid of the mixing layer with asymmetry appearing. The flux term, $\pi_\xi = \int_0^{kW} T_{\xi x}\,\mathrm{d}k^+$, shows a positive flux above and below the interface with a

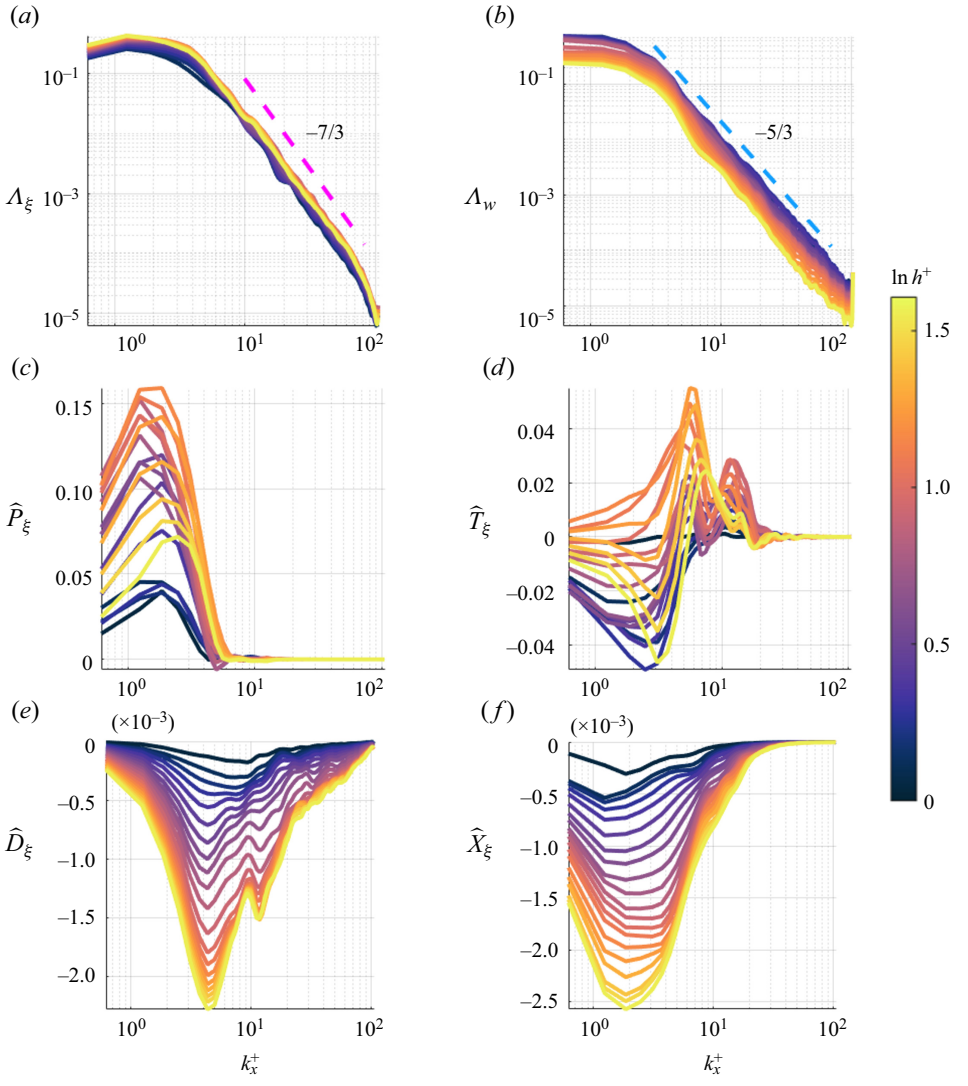

Figure 10. Time evolution of the terms in (3.8) as a function of wavenumber for the HS data set. The colour denotes the change in $\ln(h^+)$, which is the dimensionless time. The evolution of the scalar and velocity power spectra are shown for reference. Here, $\hat{P}_\xi$ is the production of scalar energy, $\hat{T}_{xi}$ is the convective transport, $\hat{D}_\xi$ is the diffusion term and $\hat{X}_\xi$ is the dissipation.

negative flux along the centreline of the mixing layer. The structures seem to correlate, and the values are comparable; however, some of the details are different.

Cook & Zhou (2002) calculate the time-varying dissipation, production and transport in non-scaling coordinates for an RTI problem. The production term of the system is very different between the RTI and RMI, so differences are expected in the temporal behaviour; however, transport and dissipation have the same mathematical structure. They do not separate terms by directionality, but comparison can be made with dominant terms. They find similar trends, with dissipation occurring at short wavelengths in the centre of the mixing layer and transport reaching peaks at long wavelengths, with positive values above and below the interface and negative values in the centre of the mixing layer.

Figure 10 shows the evolution of the terms of the spatially integrated total scalar energy transport equation (3.8) as a function of wavenumber and time. The peak of the integrated production, which is centred around the mean of the integral scales of the scalar and kinetic spectra, shows a steady growth after reshock before reaching a peak value and steadily decaying. The transport between scales is more complex. Initially, small amounts of transport occur after reshock. However, energy quickly begins being transported from large scales to small scales. Phase reversal allows a short duration of bulk transport of energy from small scales to large scales before the linear growth regime continues to drive the transport toward a profile that more closely matches an equilibrium turbulence profile such that, at the later times, energy is transporting from large scales toward the intermediate scales, and from small scales back toward intermediate scales. The LES results of Zeng *et al.* (2018) show a very similar structure for the kinetic flux term as functions of wavenumber and time. The diffusion spectrum grows with the scalar power spectrum, but its amplitude shows it to be the subdominant method of energy transport compared with the convective transport term. In this far from equilibrium setting, the dissipation spectrum shows a steadily growing peak around the peak of the production spectrum; however, it is a strongly subdominant budget term. Production is the dominant term over the whole linear growth regime, while the convective transport term steadily begins to enable transport of energy to smaller wavelengths.

5. Conclusions

The results of two sets of experiments were presented, both simultaneous PLIF and PIV, one set SS and one set time resolved. The terms in the evolution equations for the scalar and density-weighted kinetic energy spectra in a reshock RMI environment were presented. The scalar spectral index was shown, for both sets of experiments, to approximately follow the equation given by Gibson (1968) as a function of effective Schmidt number, while the kinetic energy spectral index was shown to be approximately constant over the observed effective Reynolds number range and close to the Kolmogorov $-5/3$ scaling. The partition of energy in the linear growth regime between the terms of the transport equation of the scalar power spectra was presented. A comparison of both HS and SS experiments shows a consistency of structures appearing, although IC structure dependence is suggested as a reason for the variation in the details of the evolution of the production and transport terms. This work suggests that the effective Schmidt number used here may be a useful parameter to work with to aid in the construction of spectral closure models, while the reported partitions of energy over the linear growth regime provide fields that will be useful for the comparison of RM and RT experiments at other conditions and simulations. Future work may want to expand the parameter space to see how the reported quantities behave as a function of shock strength and Atwood number.

Acknowledgements. The authors would like to thank Dr J. Herzog (now at the University of Michigan) for his invaluable assistance in the set-up of the HS laser system.

Funding. This work is supported by the US DOE/NNSA through grant number DE-NA0003932.

Declaration of interests. The authors report no conflict of interest.

Author ORCIDs.
Christopher D. Noble https://orcid.org/0000-0001-6496-5424;
Alex M. Ames https://orcid.org/0000-0001-9992-0373;
Riccardo Bonazza https://orcid.org/0000-0002-2998-7107.

Appendix. Partition of energy

The terms plotted in figure 8 are defined below. The integrals are taken from 0 to 5 where $h/h_0 = 5$ is the limit of the linear growth regime for all HS experiments

$$\left.\begin{aligned} P_\xi(z^+, k_x^+) &= \int_0^{\ln 5} \mathcal{P}\, \mathrm{d}\ln h^+ \\ \hat{P}_\xi(k_x^+, h^+) &= \int_{-\infty}^{\infty} \mathcal{P}\, \mathrm{d}z^+, \end{aligned}\right\} \tag{A1}$$

$$\left.\begin{aligned} T_{x\xi}(z^+, k_x^+) &= \int_0^{\ln 5} \mathcal{T}_{x\xi}\, \mathrm{d}\ln h^+ \\ \hat{T}_\xi(k_x^+, h^+) &= \int_{-\infty}^{\infty} \mathcal{T}_{x\xi}\, \mathrm{d}z^+, \end{aligned}\right\} \tag{A2}$$

$$\Pi_{z\xi}(z^+, k_x^+) = \int_{-\infty}^{z^+} \int_0^{\ln 5} \mathcal{T}_{z\xi}\, \mathrm{d}\ln h^+\, \mathrm{d}z^+, \tag{A3}$$

$$\left.\begin{aligned} D_{x\xi}(z^+, k_x^+) &= \int_0^{\ln 5} \mathcal{D}_{x\xi}\, \mathrm{d}\ln h^+ \\ \hat{D}_\xi(k_x^+, h^+) &= \int_{-\infty}^{\infty} \mathcal{D}_{x\xi}\, \mathrm{d}z^+, \end{aligned}\right\} \tag{A4}$$

$$D_{z\xi}(z^+, k_x^+) = \int_0^{\ln 5} \mathcal{D}_{z\xi}\, \mathrm{d}\ln h^+, \tag{A5}$$

$$\left.\begin{aligned} X_\xi(z^+, k_x^+) &= \int_0^{\ln 5} \chi_\xi\, \mathrm{d}\ln h^+ \\ \hat{X}_\xi(k_x^+, h^+) &= \int_{-\infty}^{\infty} \chi_\xi\, \mathrm{d}z^+. \end{aligned}\right\} \tag{A6}$$

References

Anderson, M.H., Puranik, B.P., Oakley, J.G., Brooks, P.W. & Bonazza, R. 2000 Shock tube investigation of hydrodynamic issues related to inertial confinement fusion. *Shock Waves* **10** (5), 377–387.

Andrade, J.R., Martins, R.S., Mompean, G., Thais, L. & Gatski, T.B. 2018 Analyzing the spectral energy cascade in turbulent channel flow. *Phys. Fluids* **30** (6), 065110.

Balasubramanian, S., Orlicz, G.C., Prestridge, K.P. & Balakumar, B.J. 2012 Experimental study of initial condition dependence on Richtmyer–Meshkov instability in the presence of reshock. *Phys. Fluids* **24** (3), 034103.

Bender, J.D., *et al*. 2021 Simulation and flow physics of a shocked and reshocked high-energy-density mixing layer. *J. Fluid Mech.* **915**, A84.

Boffetta, G. & Mazzino, A. 2017 Incompressible Rayleigh–Taylor turbulence. *Annu. Rev. Fluid Mech.* **49** (1), 119–143.

Campos, F.C. & Wouchuk, J.G. 2016 Analytical scalings of the linear Richtmyer–Meshkov instability when a shock is reflected. *Phys. Rev.* E **93** (5), 053111.

Carter, J., Pathikonda, G., Jiang, N., Felver, J.J., Roy, S. & Ranjan, D. 2019 Time-resolved measurements of turbulent mixing in shock-driven variable-density flows. *Sci. Rep.* **9** (1), 20315.

Celani, A., Cencini, M., Mazzino, A. & Vergassola, M. 2002 Active versus passive scalar turbulence. *Phys. Rev. Lett.* **89** (23), 72–106.

Celani, A., Cencini, M., Mazzino, A. & Vergassola, M. 2004 Active and passive fields face to face. *New J. Phys.* **6**, 72.

CHARONKO, J.J. & VLACHOS, P.P. 2013 Estimation of uncertainty bounds for individual particle image velocimetry measurements from cross-correlation peak ratio. *Meas. Sci. Technol.* **24** (6), 065301.

CHING, E.S.C. & CHENG, W.C. 2008 Anomalous scaling and refined similarity of an active scalar in a shell model of homogeneous turbulent convection. *Phys. Rev.* E **77** (1), 015303.

CONSTANTIN, P. 1998 Scaling exponents for active scalars. *J. Stat. Phys.* **90** (3–4), 571–595.

COOK, A.W. & ZHOU, Y. 2002 Energy transfer in Rayleigh–Taylor instability. *Phys. Rev.* E **66** (2), 026312.

CORRSIN, S. 1957 Simple theory of an idealized turbulent mixer. *AIChE J.* **3** (3), 329–330.

CORRSIN, S. 1964 The isotropic turbulent mixer: part II. Arbitrary Schmidt number. *AIChE J.* **10** (6), 870–877.

DONZIS, D.A., SREENIVASAN, K.R. & YEUNG, P.K. 2010 The batchelor spectrum for mixing of passive scalars in isotropic turbulence: submitted for the special issue dedicated to S. B. Pope. *Flow Turbul. Combust.* **85** (3–4), 549–566.

GAO, X., BERMEJO-MORENO, I. & LARSSON, J. 2020 Parametric numerical study of passive scalar mixing in shock turbulence interaction. *J. Fluid Mech.* **895**, A21.

GATTI, D., CHIARINI, A., CIMARELLI, A. & QUADRIO, M. 2020 Structure function tensor equations in inhomogeneous turbulence. *J. Fluid Mech.* **898**, A5.

GAUDING, M., WICK, A., PITSCH, H. & PETERS, N. 2014 Generalised scale-by-scale energy-budget equations and large-eddy simulations of anisotropic scalar turbulence at various Schmidt numbers. *J. Turbul.* **15** (12), 857–882.

GIBSON, C.H. 1968 Fine structure of scalar fields mixed by turbulence. II. Spectral theory. *Phys. Fluids* **11** (11), 2316–2327.

GROOM, M. & THORNBER, B. 2020 The influence of initial perturbation power spectra on the growth of a turbulent mixing layer induced by Richtmyer–Meshkov instability. *Physica* D **407**, 132463.

HAMBA, F. 2018 Turbulent energy density in scale space for inhomogeneous turbulence. *J. Fluid Mech.* **842**, 532–553.

HILL, D.J., PANTANO, C. & PULLIN, D.I. 2006 Large-eddy simulation and multiscale modelling of a Richtmyer–Meshkov instability with reshock. *J. Fluid Mech.* **557**, 29.

IYER, K.P. & YEUNG, P.K. 2014 Structure functions and applicability of Yaglom's relation in passive-scalar turbulent mixing at low Schmidt numbers with uniform mean gradient. *Phys. Fluids* **26** (8), 085107.

JAYESH & WARHAFT, Z. 1991 Probability distribution of a passive scalar in grid-generated turbulence. *Phys. Rev. Lett.* **67** (25), 3503–3506.

JOHNSON, P.L. 2020 Energy transfer from large to small scales in turbulence by multiscale nonlinear strain and vorticity interactions. *Phys. Rev. Lett.* **124** (10), 104501.

LAI, C.C.K., CHARONKO, J.J. & PRESTRIDGE, K. 2018 A Kármán–Howarth–Monin equation for variable-density turbulence. *J. Fluid Mech.* **843**, 382–418.

LINDL, J.D., AMENDT, P., BERGER, R.L., GLENDINNING, S.G., GLENZER, S.H., HAAN, S.W., KAUFFMAN, R.L., LANDEN, O.L. & SUTER, L.J. 2004 The physics basis for ignition using indirect-drive targets on the National Ignition Facility. *Phys. Plasmas* **11** (2), 339–491.

LIU, H. & XIAO, Z. 2016 Scale-to-scale energy transfer in mixing flow induced by the Richtmyer–Meshkov instability. *Phys. Rev.* E **93** (5), 053112.

MARBLE, F.E., HENDRICKS, G.J. & ZUKOSKI, E.E. 1989 Progress toward shock enhancement of supersonic combustion processes. *Turbul. Reactive Flows* **40**, 26.

MESHKOV, E.E. 1972 Instability of the interface of two gases accelerated by a shock wave. *Fluid Dyn.* **4** (5), 101–104.

MOHAGHAR, M., MCFARLAND, J. & RANJAN, D. 2022 Three-dimensional simulations of reshocked inclined Richtmyer–Meshkov instability: effects of initial perturbations. *Phys. Rev. Fluids* **7** (9), 093902.

NI, Q. 2015 Compressible turbulent mixing: effects of Schmidt number. *Phys. Rev.* E **91** (5), 053020.

NOBLE, C.D., HERZOG, J.M., AMES, A.M., OAKLEY, J., ROTHAMER, D.A. & BONAZZA, R. 2020*a* High speed plif study of the Richtmyer–Meshkov instability upon re-shock. *Physica* D **410**, 132519.

NOBLE, C.D., HERZOG, J.M., ROTHAMER, D.A., AMES, A.M., OAKLEY, J. & BONAZZA, R. 2020*b* Scalar power spectra and scalar structure function evolution in the Richtmyer–Meshkov instability upon reshock. *Trans. ASME J. Fluids Engng* **142** (12).

PAUL, I., PAPADAKIS, G. & VASSILICOS, J.C. 2018 Evolution of passive scalar statistics in a spatially developing turbulence. *Phys. Rev. Fluids* **3** (1), 014612.

PRESTRIDGE, K., RIGHTLEY, P.M., VOROBIEFF, P., BENJAMIN, R.F. & KURNIT, N.A. 2000 Simultaneous density-field visualization and PIV of a shock-accelerated gas curtain. *Exp. Fluids* **29** (4), 339–346.

REESE, D., OAKLEY, J., NAVARRO-NUNEZ, A., ROTHAMER, D., WEBER, C. & BONAZZA, R. 2014 Simultaneous concentration and velocity field measurements in a shock-accelerated mixing layer. *Exp. Fluids* **55** (10), 1823.

REILLY, D., MCFARLAND, J., MOHAGHAR, M. & RANJAN, D. 2015 The effects of initial conditions and circulation deposition on the inclined-interface reshocked Richtmyer–Meshkov instability. *Exp. Fluids* **56** (8), 168.

RICHTMYER, R.D. 1960 Taylor instability in shock acceleration of compressible fluids. *Commun. Pure Appl. Maths* **13** (2), 297–319.

RISTORCELLI, J.R. & CLARK, T.T. 2004 Rayleigh–Taylor turbulence: self-similar analysis and direct numerical simulations. *J. Fluid Mech.* **507**, 213–253.

RIVERA, M.K., DANIEL, W.B., CHEN, S.Y. & ECKE, R.E. 2003 Energy and enstrophy transfer in decaying two-dimensional turbulence. *Phys. Rev. Lett.* **90** (10), 104502.

SCHILLING, O. & LATINI, M. 2010 High-order WENO simulations of three-dimensional reshocked Richtmyer–Meshkov instability to late times: dynamics, dependence on initial conditions, and comparisons to experimental data. *Acta Mathematica* **30** (2), 595–620.

SCHILLING, O., LATINI, M. & DON, W.S. 2007 Physics of reshock and mixing in single-mode Richtmyer–Meshkov instability. *Phys. Rev.* E **76** (2), 026319.

SCHOPFLOCHER, T.P. & SULLIVAN, P.J. 2005 The relationship between skewness and kurtosis of a diffusing scalar. *Boundary-Layer Meteorol.* **115** (3), 341–358.

SEWELL, E.G., FERGUSON, K.J., KRIVETS, V.V. & JACOBS, J.W. 2021 Time-resolved particle image velocimetry measurements of the turbulent Richtmyer–Meshkov instability. *J. Fluid Mech.* **917**, A41.

THIELICKE, W. & SONNTAG, R. 2021 Particle image velocimetry for MATLAB: accuracy and enhanced algorithms in PIVlab. *J. Open Res. Softw.* **9**.

THORNBER, B. & ZHOU, Y. 2012 Energy transfer in the Richtmyer–Meshkov instability. *Phys. Rev.* E **86** (5), 056302.

TRITSCHLER, V.K., OLSON, B.J., LELE, S.K., HICKEL, S., HU, X.Y. & ADAMS, N.A. 2014 On the Richtmyer–Meshkov instability evolving from a deterministic multimode planar interface. *J. Fluid Mech.* **755**, 429–462.

VERMA, M.K., KUMAR, A., KUMAR, P., BARMAN, S., CHATTERJEE, A.G. & SAMTANEY, R. 2018 Energy spectra and fluxes in dissipation range of turbulent and laminar flows. *Fluid Dyn.* **53**, 862–873.

WEBER, C.R., HAEHN, N.S., OAKLEY, J.G., ROTHAMER, D.A. & BONAZZA, R. 2014 An experimental investigation of the turbulent mixing transition in the Richtmyer–Meshkov instability. *J. Fluid Mech.* **748**, 457–487.

YEUNG, P.K. & SREENIVASAN, K.R. 2013 Spectrum of passive scalars of high molecular diffusivity in turbulent mixing. *J. Fluid Mech.* **716**, R14.

YEUNG, P.K. & SREENIVASAN, K.R. 2014 Direct numerical simulation of turbulent mixing at very low Schmidt number with a uniform mean gradient. *Phys. Fluids* **26** (1), 015107.

ZENG, W.-G., PAN, J.-H., SUN, Y.-T. & REN, Y.-X. 2018 Turbulent mixing and energy transfer of reshocked heavy gas curtain. *Phys. Fluids* **30** (6), 064106.

ZHOU, Y. 2017*a* Rayleigh–Taylor and Richtmyer–Meshkov instability induced flow, turbulence, and mixing. I. *Phys. Rep.* **720–722**, 1–136.

ZHOU, Y. 2017*b* Rayleigh–Taylor and Richtmyer–Meshkov instability induced flow, turbulence, and mixing. II. *Phys. Rep.* **723–725**, 1–160.

ZHOU, Z., DING, J., CHENG, W. & LUO, X. 2023 Scaling law of structure function of Richtmyer–Meshkov turbulence. *J. Fluid Mech.* **972**, A18.